Title	Synergetic approach to achieve enhanced lithium ion storage performance in ternary phased SnO2–Fe2O3/rGO composite nanostructures
Author(s)	Zhu, Jixin; Lu, Ziyang; Oo, Moe Ohnmar; Hng, Huey Hoon; Ma, Jan; Zhang, Hua; Yan, Qingyu
Citation	Zhu, J., Lu, Z., Oo, M. O., Hng, H., H., Ma, J., Zhang, H., et al. (2011). Synergetic approach to achieve enhanced lithium ion storage performance in ternary phased SnO2–Fe2O3/rGO composite nanostructures. Journal of Materials Chemistry, 21, 12770-12776.
Date	2011
URL	http://hdl.handle.net/10220/8408
Rights	© 2011 The Royal Society of Chemistry. This is the author created version of a work that has been peer reviewed and accepted for publication by Journal of Materials Chemistry, The Royal Society of Chemistry. It incorporates referee's comments but changes resulting from the publishing process, such as copyediting, structural formatting, may not be reflected in this document. The published version is available at: http://dx.doi.org/10.1039/c1jm12447a.

Journal of Materials Chemistry

Dynamic Article Links

Cite this: DOI: 10.1039/c0xx00000x

www.rsc.org/xxxxxx

ARTICLE TYPE

Synergetic approach to achieve enhanced lithium ion storage performance in ternary phased SnO_2–Fe_2O_3/rGO composite nanostructures†

Jixin Zhu,[a] Ziyang Lu,[a] Moe Ohnmar Oo,[a] Huey Hoon Hng,[a] Jan Ma,[a] Hua Zhang[a] and Qingyu Yan*[abc]

Received (in XXX, XXX) Xth XXXXXXXXX 20XX, Accepted Xth XXXXXXXXX 20XX
DOI: 10.1039/b000000x

We report here a study on the Li ion storage performance of binary phased SnO_2/rGO and ternary phased SnO_2–Fe_2O_3/rGO composite nanostructures. The SnO_2/rGO and SnO_2–Fe_2O_3/rGO were prepared by a facile wet-chemical approach. The Li storage performances of these samples were closely related to the weight ratio of SnO_2 : rGO or SnO_2 : Fe_2O_3 : rGO. It was found that ternary SnO_2–Fe_2O_3/rGO composite nanostructures (*e.g.* with a weight ratio of SnO_2 : Fe_2O_3 : rGO = 11 : 1 : 13) showed significant enhancement of the specific capacities and cyclabilities as compared to that of SnO_2/rGO samples. For example, the SnO_2–Fe_2O_3/rGO electrode depicted a specific capacity of 958 mA h g^{-1} at a current density of 395 mA g^{-1} (0.5 C) during the 100th cycle. Such Li storage performances of the SnO_2–Fe_2O_3/rGO electrodes, especially at high current densities (*e.g.* 530 mA h g^{-1} at 5 C rate), were also much better than those reported for either SnO_2-based or Fe_2O_3-based electrodes. Such a synergetic effect in the SnO_2/Fe_2O_3/rGO composite nanostructures is promising for the development of advanced electrode materials for rechargeable Li-ion batteries.

Introduction

The lithium ion battery, as an effective electrochemical energy storage device, has attracted much interest recently. Great efforts have been devoted to develop different types of materials with high reversible capacity, long cycle life, and low cost.[1–7] Electrochemically active metal oxides such as SnO_2, Fe_2O_3, and Co_3O_4, MnO_2 have long been considered as promising anode materials for lithium ion batteries because of their higher theoretical capacities and high energy densities than those of conventional graphite anodes (372 mA h g^{-1}).[8–12] However, these materials suffer from poor stability due to the pulverization process.[3,13–15] Although efforts have been taken to improve the cyclability and specific capacity through nanostructuring transition metal oxides,[8] preservation of high capacities under high current density remains an important challenge due to the aggregation of the nanostructures and the collapse of their crystal structures during the insertion and extraction of Li ions.[3,16–19] Combining metal oxides with conducting matrixes, *e.g.* amorphous carbon shell, carbon nanotubes or graphene sheets, to preserve their nanostructures has been reported to be an effective route to overcome these problems.[1,20–26] For example, a high reversible capacity of 800 mA h g^{-1} at a discharge current density of 50 mA g^{-1} can be delivered through inducing Co_3O_4 on graphene,[1] and a reversible specific capacity approaching 1026 mA h g^{-1} at a discharge current density of 35 mA g^{-1} can be retained after encapsulating Fe_3O_4 in graphene sheets; anatase TiO_2/rGO composites give a capacity as high as 96 mA h g^{-1} at 30 C and the Mn_3O_4 nanoparticles formed on rGO show a high specific capacity up to 900 mA h g^{-1}, near their theoretical capacity, with good rate capability and cycling stability.[5,27,28] Here, graphene or rGO served as either a flexible, high conductive matrix to maintain the electrical contact from the metal oxide nanoparticles to the current collectors or a buffer to prevent the agglomeration of nanoparticles.[29]

SnO_2, as one of the most promising anode electrode materials, has attracted great interest. During the charge/discharge process, there are two typical electrochemical processes taking place in SnO_2: (1) $SnO_2 + 4Li^+ + 4e^- \rightarrow Sn + 2Li_2O$; (2) $Sn + xLi^+ + xe^- \leftrightarrow Li_xSn$ ($0 \leq x \leq 4.4$).[8,30] Based on the second reaction, SnO_2 exhibits an attractive theoretical capacity (*e.g.* 790 mA h g^{-1}) as compared to that of the current graphitic material (*e.g.* 372 mA h g^{-1}). However, a large volume swing (about 358%) occurs during the Li intercalation process in SnO_2,[31] leading to the pulverization of Sn particles and the rapid capacity decay because of the loss of electrical contact with the current collector.[30,32–34]

To solve this issue, advanced preparation processes of SnO_2 have been developed with controlled size, structure, composition and shape.[4,35–37] There are also efforts to mix SnO_2 with other

[a]*School of Materials Science and Engineering, Nanyang Technological University, 50 Nanyang Avenue, Singapore, 639798, Singapore. E-mail: alexyan@ntu.edu.sg*
[b]*Energy Research Institute@NTU, Nanyang Technological University, Singapore, 637459, Singapore*
[c]*TUM CREATE Centre for Electromobility, Nanyan Technological University, Singapore, 637459, Singapore*

† Electronic supplementary information (ESI) available: Detailed characterization data including Raman, TGA, SEM, elemental mapping, XRD, EDX, TEM, charge–discharge voltage profiles and Table S1. See DOI: 10.1039/c1jm12447a

metal oxides, *e.g.* In_2O_3, to induce synergistic effects.[38,39] High reversible capacities, in particular at high C rates, are still desired in these SnO_2 based anodes even though improved Li storage performances have been demonstrated. To achieve high reversible capacities at high current densities, the electrode material is generally required to (1) remain as nanostructures without significant agglomeration to facilitate the fast Li diffusion process and (2) maintain electrical contact with the current collectors. SnO_2 has been attached onto conductive materials, *e.g.* amorphous carbon, carbon nanotubes and reduced graphene oxide (rGO) sheets,[5,22,40–44] to help maintain the electrical contact, and has shown enhanced reversible capacities at reasonable C rates. Further improvement of this concept to achieve high Li storage performance at higher C rates is attractive.

Herein, we report a facile one-step route to prepare ternary phased SnO_2–Fe_2O_3/rGO composite nanostructures with excellent Li storage performances. It was revealed that adding a small amount of amorphous Fe_2O_3 NPs (*e.g.* 4 wt%) into the SnO_2/rGO composite nanostructures resulted in much improved reversible capacities and cycling stabilities, especially at high current densities. The Li storage performance of SnO_2–Fe_2O_3/rGO electrodes was much better than those reported for SnO_2- or Fe_2O_3-based anode materials.[26,31,45,46]

The high resolution transmission electron microcopy (HRTEM) observation indicated that there was no obvious agglomeration of the SnO_2 nanoparticles (NPs) in the ternary phased SnO_2–Fe_2O_3/rGO sample while agglomeration of the SnO_2 NPs was noted in the binary SnO_2/rGO sample. The uniform mixing of amorphous Fe_2O_3 NPs with SnO_2 NPs on the rGO sheets may effectively prevent the agglomeration of SnO_2 during the charge–discharge process, as illustrated in Scheme 1. The large specific surface area was maintained in the electrode to facilitate fast Li ion diffusion and led to the enhanced Li storage performance at high current densities. Such synergetic approaches in the SnO_2–Fe_2O_3/rGO composite nanostructures could be promising for the development of advanced electrodes for the rechargeable Li ion battery.

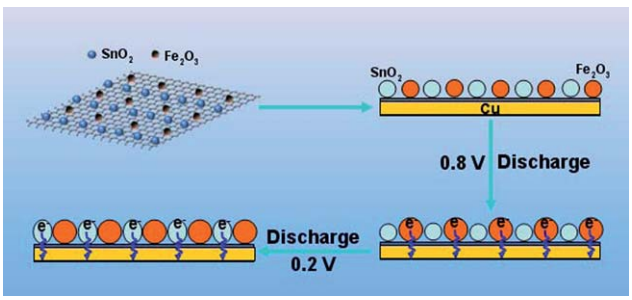

Scheme 1 Schematic diagram illustrates the possible mechanism for preventing the agglomeration of SnO_2 nanoparticles (NPs) in the SnO_2–Fe_2O_3/rGO composite during the discharging process. The Li intercalation of Fe_2O_3 takes place at a higher voltage (*e.g.* ~0.8 V) than that of SnO_2 (*e.g.* 0.2 V). Therefore, during the discharge process, the Fe_2O_3 NPs were lithiated and expanded first, which might effectively limit the SnO_2 NPs from being in contact with each other and prevent their agglomeration.

Experimental

Synthesis of the graphite oxide

Graphite oxide was synthesized from natural graphite (SP-1) by a modified Hummer's method.[45,47,48] In brief, 1.5 g graphite powder was added into a mixture of 10 mL 98% H_2SO_4, 1.25 g $K_2S_2O_8$, and 1.25 g P_2O_5, and the solution was maintained at 80 °C for 4.5 h. The resulting pre-oxidized product was cleaned using water and dried in a vacuum oven at 50 °C. After it was mixed with 60 mL 98% H_2SO_4, 7.5 g $KMnO_4$ was slowly added at a temperature below 20 °C, and then followed by 125 mL H_2O. After 2 h, additional 200 mL H_2O and 10 mL 30% H_2O_2 were slowly added into the solution to completely react with the excess $KMnO_4$. After 10 minutes, a bright yellow solution was obtained. The resulting mixture was washed with diluted HCl aqueous (1/10 v/v) solution and H_2O. The graphite oxide was obtained after drying in a vacuum oven at 30 °C.

Synthesis of SnO_2/rGO composite nanostructures

In a typical procedure, 50 mg graphite oxide was dispersed in 70 mL 99.9% ethanol by sonication to get graphene oxide (GO) sheets. Then, x mg $SnCl_2$ (where x is 55, 182 and 364 to get SnO_2/rGO with $I_{SnO_2/rGO} = 0.39 : 1$, $0.96 : 1$ and $1.78 : 1$, respectively) was added into the solution. The mixture was sealed in a Teflon-lined autoclave and maintained at 170 °C for 4 h. After it was cooled down to room temperature, the precipitate, *e.g.* SnO_2/rGO, was collected and washed with ethanol. The weight ratio of SnO_2 to rGO was calculated from TGA analysis results.

Synthesis of SnO_2–Fe_2O_3/rGO composite nanostructures

In a typical procedure, 50 mg graphite oxide was dispersed in 70 mL 99.9% ethanol by sonication to get graphene oxide (GO) sheets. Then, x mg $SnCl_2$ and y mg $FeCl_2$ were added into the solution (detailed x and y are listed in Table S1†). The mixture was sealed in a Teflon-lined autoclave and maintained at 170 °C for 4 h. After it was cooled down to room temperature, the precipitate, *e.g.* SnO_2–Fe_2O_3/rGO, was collected and washed with ethanol. The weight ratios of precursors and resultant samples were calculated from TGA analysis and EDX results, and the results are presented in ESI, Table S1†.

Material characterization

The morphology of the as-synthesized samples was investigated by using a field emission SEM (JEOL JSM-7600F). For TEM observation, the suspension was dropped onto carbon coated copper grids and dried at room temperature. A TEM (JEOL JEM-2100) operating at 200 kV was used to characterize the nanostructures. Crystal phases were identified using a Scintag PAD-V X-ray diffractometer with Cu Kα irradiation. Raman spectra were obtained with a WITec CRM200 confocal Raman microscopy system with a laser wavelength of 488 nm and a laser spot size of 0.5 mm. The Si peak at 520 cm^{-1} was used as a reference for wavenumber calibration. Thermogravimetry analysis (TGA, Q500) was carried out in the temperature range of 25 to 700 °C at a heating rate of 10 °C min^{-1} in air. X-Ray Photoelectron Spectroscopy (XPS) of the resulting composites was performed with an

X-ray photoelectron spectrometer (Kratos AXIS Ultra) using monochromatic Al Kα (1486.71 eV) X-ray radiation (15 kV and 10 mA); 160 eV pass energy was used for survey scan, whereas 40 eV was used for the high-resolution scan.

Electrochemical measurements

The metal oxide/rGO (MO/rGO) composite nanostructures were annealed at 150 °C for 30 min under Ar atmosphere. Then, 80 wt % active material (SnO_2/rGO or SnO_2–Fe_2O_3/rGO), 10 wt% acetylene black (Super-P), and 10 wt% polyvinylidene fluoride (PVDF) binder were mixed into *N*-methyl-2-pyrrolidinone (NMP). The obtained slurry was coated onto Cu foil and a stainless steel blade was then used to achieve a uniform film, which was finally dried in vacuum at 50 °C for 12 h to remove the solvent, and finally used as working electrode. Electrochemical measurements were carried out on CR2032 (3 V) coin-type cells with lithium metal as the counter/reference electrode, Celgard 2400 membrane as the separator, and the electrolyte solution obtained by dissolving 1 M $LiPF_6$ into a mixture of ethylene carbonate (EC) and dimethyl carbonate (DMC) (EC/DMC, 50 : 50 w/w). The coin cells were assembled in an Ar-filled glovebox with concentrations of moisture and oxygen below 1.0 ppm. The charge/discharge tests were performed with a NEWARE battery tester at a voltage window of 0.001–3.0 V for SnO_2/rGO and SnO_2–Fe_2O_3/rGO samples. Cyclic voltammetry (0.001–3 V, 0.5 mV s^{-1}) was performed with an electrochemical workstation (CHI 660C).

Results and discussion

Reacting $SnCl_2$ with GOs in the solvothermal process led to the formation of composite nanostructures with NPs decorated onto thin GO sheets as revealed by TEM observations (see Fig. 1). Fine particles with the size of 2–4 nm were uniformly attached onto the surface of the GO nanosheets (see Fig. 1a and b). This was induced by the heterogeneous nucleation process of NPs on the graphene oxide sheets. The reduction of the GOs to reduced graphene oxide (rGO) was confirmed by Raman spectroscopy (see ESI, Fig. S1†). The Raman spectroscopy results showed an increase in the intensity ratio ($I_{D:G}$) between the D band (located at 1350 cm^{-1}) and G band (located at 1580 cm^{-1}), *e.g.* $I_{D:G} = 0.98$ for GO sheets increased to $I_{D:G} = 1.02$ for the SnO_2/rGO sample. This confirmed the reduction of GOs through the solvothermal process, which agreed well with previous reports.[45] The ring patterns (see Fig. 1c) obtained in the selected area electron diffraction (SAED) measurements revealed that the NPs on the rGO sheets were tetragonal SnO_2 (JCPDF77-0452), which was consistent with the HRTEM observation (see Fig. 1d). The mass loading of the SnO_2 on the rGO sheets (defined as the weight ratio of SnO_2 and rGO, $I_{SnO_2:rGO}$) could be tailored by changing the weight ratio between $SnCl_2$ and GOs in the solvothermal process as indicated by the TGA results (see ESI, Fig. S2†). For example, $I_{SnO_2:rGO}$ could be tuned from 0.39 : 1 to 1.78 : 1 by changing the weight ratio of $SnCl_2$: GOs from 1.10 : 1 to 7.28 : 1 as revealed by the TGA measurements. Increasing the mass loading of the SnO_2 on rGO sheets led to the partial agglomeration of the NPs (see ESI, Fig. S3a–c†). Here, it is worth pointing out that the mass loading of the metal oxide NPs on rGO sheets may affect their energy storage performance as indicated in a previous report.[49]

Adding $FeCl_2$ to the solvothermal process resulted in samples with similar morphology as that of SnO_2/rGO composite nanostructures (see Fig. 1e and f). It was observed that nanoparticles with the size of 2–4 nm were uniformly attached onto the surface of rGO sheets. The EDX elemental mapping results of Sn and Fe

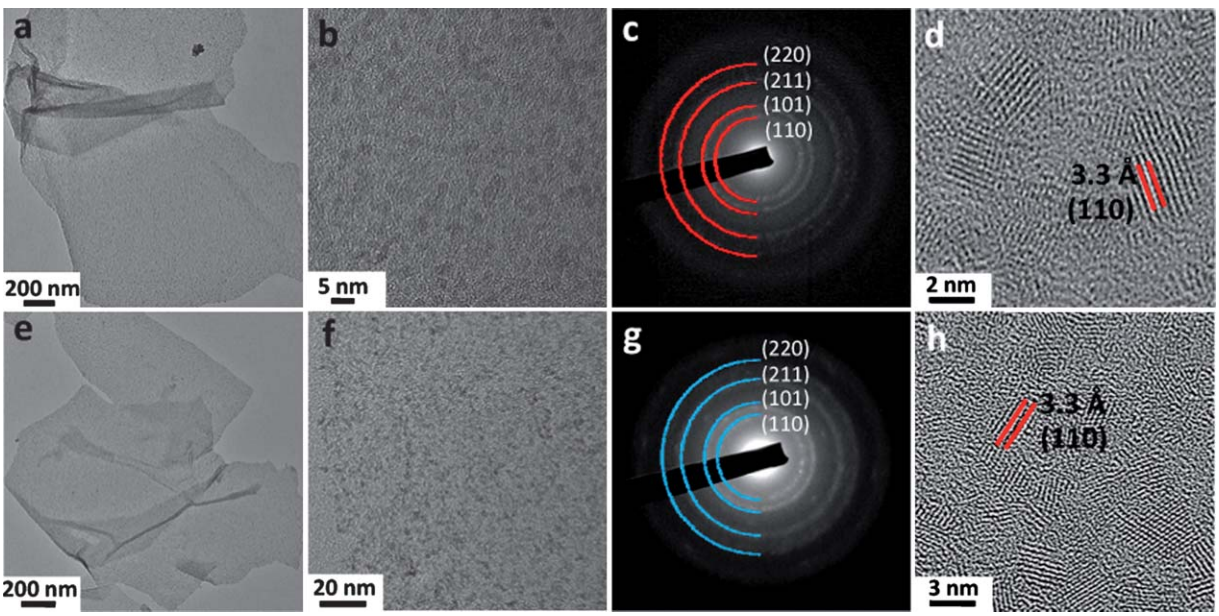

Fig. 1 (a) Low and (b) high magnification TEM images of the SnO_2/rGO composite nanostructures prepared with a precursor weight ratio of $SnCl_2$: GOs = 1.10 : 1; (c) SAED pattern and (d) HRTEM of SnO_2 NPs in SnO_2/rGO sample; (e) low magnification TEM image, (f) high magnification TEM image, (g) SAED pattern and (h) HRTEM image of the composite nanostructures prepared with a precursor weight ratio of $SnCl_2$: $FeCl_2$: GOs = 3.64 : 2 : 1.

(see ESI Fig. S4†) indicated the homogeneous distribution of Fe and Sn elements on the rGO sheets. The well-crystallized SnO_2 lattice could be identified in the HRTEM image (see Fig. 1g). However, the ring pattern (see Fig. 1g) obtained in the selected area electron diffraction (SAED) measurements (see Fig. 1h) corresponds to only tetragonal SnO_2 (JCPDF77-0452) without detectable Fe containing phases. This was also confirmed by the XRD measurements (see ESI, Fig. S5†). The XRD patterns of Fe containing SnO_2/rGO samples showed only peaks corresponding to the tetragonal SnO_2 phase. The crystal size of SnO_2 was estimated to be 2–3 nm from the width of peaks in the XRD patterns using Scherrer's equation, which was consistent with the HRTEM observations (see Fig. 1h).

In order to obtain insights into the Fe compound formation, we acquired core-level XPS spectra (see Fig. 2) from samples prepared with a precursor weight ratio of $SnCl_2$: $FeCl_2$: GOs = 3.64 : 2 : 1. The C 1s sub-band (Fig. 2a) showed a strong peak of sp^2 carbon and a weak peak of carbonyl groups, which correspond well with those reported for rGO sheets.[50,51] The formation of SnO_2 was revealed by Sn $3d_{3/2}$ and $3d_{5/2}$ bands at 494.0 and 485.5 eV, which agreed with the SAED and XRD results. Both the Fe 2p bands (*e.g.* the Fe $2p_{3/2}$ at 711 eV and Fe $2p_{1/2}$ at 724 eV, see Fig. 2c) and Fe 3p band at 56.06 eV (see Fig. 2d) indicated the formation of Fe_2O_3.[31,32,52] Here, it was noted that there was no detectable chlorine element in the EDX spectra of the annealed Fe containing SnO_2/rGO samples (see ESI, Fig. S6†), which excluded the possible formation of $FeCl_3$ on the rGO sheets.

Based on the above results, it was concluded that amorphous Fe_2O_3 nanoparticles were formed in the samples prepared from $SnCl_2$, $FeCl_2$ and GOs. The morphologies of the resultant sample had no obvious change (see ESI, Fig. S7†) as compared to those of SnO_2/rGO samples. The weight ratios of SnO_2, Fe_2O_3 and rGO, $I_{SnO_2:Fe_2O_3:rGO}$, in the final samples were characterized by TGA and EDX (see ESI, Fig. S6 and S8 summarized in Table S1†), which closely related to the weight ratios of the precursors. For example, samples with $I_{SnO_2:Fe_2O_3:rGO}$ = 11 : 1 : 13 were obtained with a precursor weight ratio of $SnCl_2$: $FeCl_2$: GOs = 3.64 : 2 : 1. Changing the precursor weight ratio to $SnCl_2$: $FeCl_2$: GOs = 0.78 : 4 : 1 led to the formation of samples with $I_{SnO_2:Fe_2O_3:rGO}$ = 1.32 : 1 : 1.68.

To study the Li-ion storage performance of these SnO_2/rGO and SnO_2–Fe_2O_3/rGO composite nanostructures, a series of electrochemical measurements were carried out based on the half-cell configuration.[45,53] The cyclic voltammetry (CV) curves of these samples (see Fig. 3) were obtained at a scanning rate of 0.5 mV s^{-1} over the voltage range of 0.001–3.0 V. The first cathodic scans of the SnO_2/rGO composite nanostructures with $I_{SnO_2:rGO}$ = 0.96 : 1 showed four reduction peaks (see Fig. 3a), which were consistent with previous reports.[41,54] The peaks at around 2.27 V and 1.39 V were ascribed to the formation of the solid electrolyte interface (SEI) while the peak at 0.76 V was attributed to the reduction of SnO_2 to Sn and Li_2O.[31] The reduction peak in the range of 0 to 0.7 V was mainly associated with the insertion of Li into metallic Sn and carbon materials[41,54] corresponding to the following reactions: (1) Sn + $x$$Li^+$ + xe^- ↔ Li_xSn ($0 \le x \le 4.4$) and (2) $x$$Li^+$ + C (graphene) + xe^- ↔ Li_xC. For SnO_2–Fe_2O_3/rGO composite nanostructures, new reduction peaks were observed (see Fig. 3b–d). The peaks at 1.67, 1.27 and 0.84 V were attributed to the insertion of Li^+ into Fe_2O_3.[3] The broad reduction peak at around 0.17 V was ascribed to the formation of Li_xSn.[34,55]

The charge–discharge cycling performances of the SnO_2/rGO and SnO_2–Fe_2O_3/rGO composite nanostructures were investigated at a high current density of 395 mA g^{-1} (0.5 C) within the voltage range of 0.001 to 3.0 V (see Fig. 4). For SnO_2/rGO composite nanostructures with different $I_{SnO_2:rGO}$ values, the cycling performance varied (see Fig. 4a). For example, SnO_2/rGO composite nanostructures with $I_{SnO_2:rGO}$ = 0.96 : 1 showed

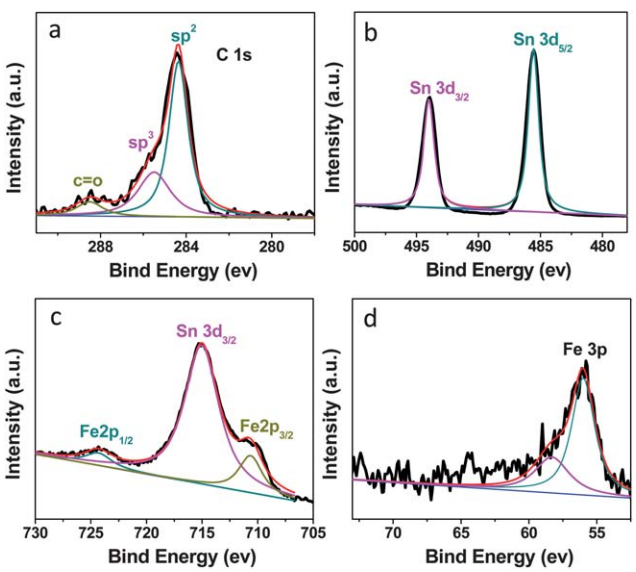

Fig. 2 XPS spectra for composite nanostructure prepared with a precursor weight ratio of $SnCl_2$: $FeCl_2$: GOs = 3.64 : 2 : 1, which show core-level (a) C 1s, (b) Sn 3d, (c) Sn 3p and Fe 2p, (d) Fe 3p bands. The bold black curves are experimental data; the thinner coloured curves are deconvoluted sub-band components.

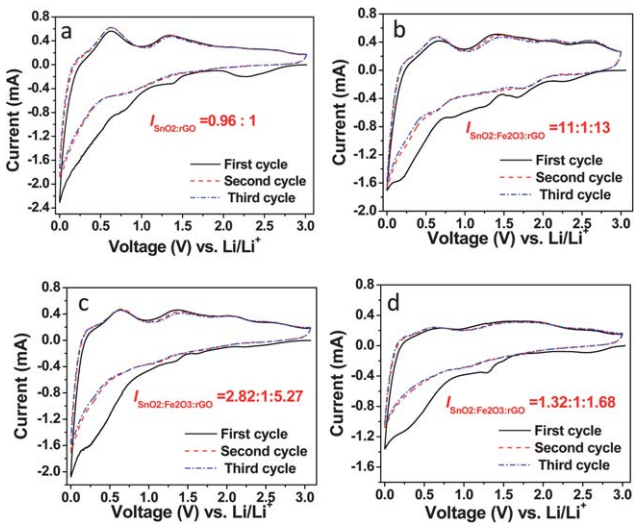

Fig. 3 Cyclic voltammetry (CV) curves of (a) SnO_2/rGO and (b–d) SnO_2–Fe_2O_3/rGO samples at a scanning rate of 0.5 mV s^{-1} in the voltage range of 0.001–3.0 V.

a discharge capacity of 816 mA h g^{-1} at 0.5 C during the 12th cycle. The capacities of the sample with $I_{SnO_2:rGO} = 0.96:1$ at 0.5 C decreased gradually and reached 420 mA h g^{-1} during the 100th cycle. Samples with a lower $I_{SnO_2:rGO}$ value, *e.g.* 0.39 : 1, showed a lower discharge capacity of 445 mA h g^{-1} at 0.5 C during the 12th cycle, which remained relatively stable at 270 mA h g^{-1} during the 100th cycle. For SnO_2/rGO samples with a higher $I_{SnO_2:rGO}$ value (*e.g.* 1.78 : 1), the specific capacity at 0.5 C was 833 mA h g^{-1} during the 12th cycle, which dropped rapidly and reached 274 mA h g^{-1} during the 100th cycle. The relatively stable cycling performance for samples with lower $I_{SnO_2:rGO}$ values (*e.g.* 0.39 : 1 or 0.96 : 1) was mainly attributed to less agglomeration of the SnO_2 NPs during the charge–discharge cycling process, which maintained the large surface area of the SnO_2 NPs to facilitate the effective Li ion diffusion. However, the low mass loading of SnO_2 in the samples with $I_{SnO_2:rGO} = 0.39:1$ led to low effective specific capacities[33,40] because the theoretical capacity of SnO_2 is much higher than that of rGO sheets. On the other hand, high mass loading of SnO_2 in samples with $I_{SnO_2:rGO} = 1.78:1$ could result in a high effective specific capacity. But the high density of SnO_2 NPs on rGO sheets tend to agglomerate during the charge–discharge cycling process and led to the rapid drop in the reversible capacities. Samples with the proper $I_{SnO_2:rGO}$ ratio (*e.g.* 0.96 : 1) showed better Li storage performance than the other two samples with either higher or lower $I_{SnO_2:rGO}$ values. However, further improvement is still desired.

The charge–discharge cycling performance of SnO_2–Fe_2O_3/rGO samples was also investigated. It was found that incorporating only small amounts of amorphous Fe_2O_3 NPs into the composite nanostructures led to much improved Li storage performance. For example, SnO_2–Fe_2O_3/rGO samples with $I_{SnO_2:Fe_2O_3:GO} = 11:1:13$ showed a high reversible capacity of

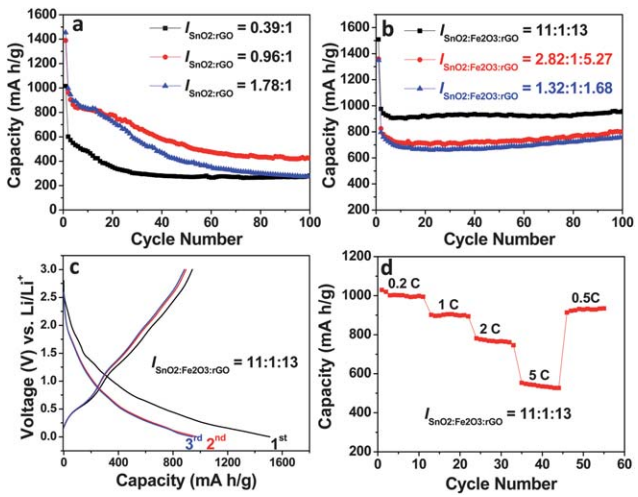

Fig. 4 (a) Cycling performance of the SnO_2/rGO electrodes at a current density of 0.5 C (395 mA g^{-1}) within a voltage window of 0.001–3.0 V; (b) cycling performance of the SnO_2–Fe_2O_3/rGO electrodes at a current density of 0.5 C (395 mA g^{-1}) within a voltage window of 0.001–3.0 V; (c) charge–discharge voltage profiles of the SnO_2–Fe_2O_3/rGO with $I_{SnO_2:Fe_2O_3:rGO} = 11:1:13$ for the first three cycles at a current density of 0.5 C (395 mA g^{-1}); (d) cycling performance of the SnO_2–Fe_2O_3/rGO with $I_{SnO_2:Fe_2O_3:rGO} = 11:1:13$ at various C rates. Here, 1 C is equal to 790 mA g^{-1}.

976 mA h g^{-1} (Fig. 4b) during the second cycle at 0.5 C (395 mA g^{-1}), which also showed excellent cycling stability and maintained at 958 mA h g^{-1} during the 100th cycle. Such performance was much better than our measured data for SnO_2/rGO electrodes as well as those reported for SnO_2 based electrodes[31,34,55,56] at relatively high current densities, *e.g.* 395 mA g^{-1} (0.5 C). It is also worth pointing out that such Li ion storage properties were also better than those reported for Fe_2O_3 based Li ion battery anodes.[3,46,57–59] When increasing the amount of amorphous Fe_2O_3 in the sample, we found that the reversible capacities of the SnO_2–Fe_2O_3/rGO electrodes decreased. For example, samples with $I_{SnO_2:Fe_2O_3:rGO} = 2.82:1:5.27$ and 1.32 : 1 : 1.68 depicted specific capacities of 825 mA h g^{-1} and 797 mA h g^{-1}, respectively, during the second charge–discharge cycle at 0.5 C (395 mA g^{-1}). Here, the decreased specific capacities measured in these samples with a higher weight percentage of amorphous Fe_2O_3 were mainly due to the low specific capacities of amorphous Fe_2O_3. Although specific capacities decreased, the samples with an increased amount of Fe_2O_3 still showed excellent cyclability during the charge–discharge process, *e.g.* samples with $I_{SnO_2:Fe_2O_3:rGO} = 2.82:1:5.27$ and 1.32 : 1 : 1.68 depicted specific capacities of 801 and 758 mA h g^{-1} at 0.5 C during the 100th cycle, respectively. These performances were still much better than those measured for SnO_2/rGO samples with different $I_{SnO_2:rGO}$ values. The capacity curve showed an upward trend, which indicated an activation process in the electrode material.[30]

Fig. 4c showed the charge–discharge voltage profiles of the SnO_2–Fe_2O_3/rGO electrodes with $I_{SnO_2:Fe_2O_3:rGO} = 11:1:13$ for the first three cycles at a current rate of 0.5 C, which was similar to that of other SnO_2–Fe_2O_3/rGO electrodes with different $I_{SnO_2:Fe_2O_3:rGO}$ values (see ESI, Fig. S9†), *e.g.* $I_{SnO_2:Fe_2O_3:rGO} = 2.82:1:5.27$ and 1.32 : 1 : 1.68. The potential plateaus observed in the discharge curves were consistent with the CV results. The insertion process gave a first discharge capacity of 1509 mA h g^{-1} and a subsequent charge capacity of 941 mA h g^{-1}, showing a Coulombic efficiency of 62.4%. During the second cycle, the discharge capacity decreased to 976 mA h g^{-1} with a corresponding charge capacity of 896 mA h g^{-1}, leading to a much higher Coulombic efficiency of 91.8%.

The cycling responses of the SnO_2–Fe_2O_3/rGO electrodes with $I_{SnO_2:Fe_2O_3:rGO} = 11:1:13$ were also evaluated at different C rates as shown in Fig. 4d. The sample showed a high capacity of 1000 mA h g^{-1} at 0.2 C, which changed to 900 and 770 mA h g^{-1} at 1 and 2 C, respectively. It could also depict a capacity as high as 540 mA h g^{-1} even at 5 C (3950 mA g^{-1}) rate. These performances at high C rates, especially at 5 C, were better than those reported for either SnO_2- or Fe_2O_3-based anode materials.[26,31,45,46] For example, the SnO_2/rGO composites obtained by a microwave route depicted a discharge capacity of 600 mA h g^{-1} after 50 charge–discharge cycles and decreased to 550 mA h g^{-1} after 100 charge–discharge cycles. Iron oxide-based nanotube arrays were prepared by a template route and delivered a capacity of 659 mA h g^{-1} after 150 charge–discharge cycles. These Li storage performances were lower than those of the SnO_2–Fe_2O_3/rGO electrodes.

Here, the excellent Li storage properties of the SnO_2–Fe_2O_3/rGO electrodes at high C rates are proposed to be due to the following factors. In general, Li storage performance requires (1)

a fast and effective Li ion diffusion path in the electrodes; and (2) a reliable electrical contact between individual active material components (*e.g.* each SnO_2 particle) and the current collectors; in order to achieve high specific capacitance and stable cycling performance at high current densities. The rGO sheets in the SnO_2–Fe_2O_3/rGO composite nanostructures could serve as the conductive scaffolds[7] to maintain the reliable electrical contacts between SnO_2/Fe_2O_3 with the current collectors. On the other hand, the amorphous Fe_2O_3 may prevent SnO_2 NPs on the rGO sheets from agglomerating during the charge–discharge process to maintain a large specific surface area for Li ion intercalation. As indicated by the above EDS results (see ESI, Fig. S4†), the amorphous Fe_2O_3 and SnO_2 were homogeneously mixed with each other on the rGO surface. The Li intercalation of Fe_2O_3 occurs at a higher voltage (*e.g.* ~0.8 V) than that of SnO_2 (*e.g.* 0.2 V). Therefore, during the discharge process, the Fe_2O_3 NPs were lithiated and expanded first. This may favor the formation of barriers to prevent the agglomeration of SnO_2 NPs as illustrated in Scheme 1. Otherwise, the agglomeration of SnO_2 NPs may hinder the effective diffusion of Li ions and result in decreased reversible capacities, which was observed in the SnO_2/rGO samples. Our HRTEM measurements showed that the SnO_2 in the SnO_2–Fe_2O_3/rGO remained as 5–8 nm particles (see ESI, Fig. S10a†) after the 100 charge–discharge cycles while obvious agglomeration of the SnO_2 was observed in SnO_2/rGO electrodes after 100 charge–discharge cycles (see ESI, Fig. S10b†).

Conclusions

In summary, binary phased (*e.g.* SnO_2/rGO) and ternary phased (*e.g.* SnO_2–Fe_2O_3/rGO) composite nanostructures with a controlled phase ratio were prepared by a facile environment-friendly approach. The Li ion storage properties of the SnO_2/rGO could be adjusted by changing the weight ratio of SnO_2 : rGO. Significant improvements in the Li storage performances, especially at high current densities (*e.g.* 5 C), were achieved by adding a small amount of amorphous Fe_2O_3 NPs into the SnO_2/rGO. Although the amorphous Fe_2O_3 NPs were not expected to contribute much to the total specific capacity of the SnO_2–Fe_2O_3/rGO electrode, they may help to effectively prevent the agglomeration of SnO_2 NPs on the rGO sheets as indicated by our HRTEM observation. Such a synergetic approach can be extended to other material systems and lead to promising routes to develop advanced electrode materials for rechargeable Li-ion batteries.

Acknowledgements

The authors gratefully acknowledge AcRF Tier 1 RG 31/08 of MOE (Singapore), NRF2009EWT-RP001-026 (Singapore), A*STAR SERC grant 1021700144, AcRF Tier 2 (MOE2010-T2-1-017) from MOE (Singapore) and Singapore MPA 23/04.15.03 grant. H.Z. thanks the support of AcRF Tier 2 (ARC 10/10, No. MOE2010-T2-1-060) from MOE in Singapore and the New Initiative fund FY 2010 (M58120031) from NTU, Singapore.

References

1 Z. S. Wu, W. C. Ren, L. Wen, L. B. Gao, J. P. Zhao, Z. P. Chen, G. M. Zhou, F. Li and H. M. Cheng, *ACS Nano*, 2010, **4**, 3187–3194.
2 P. Poizot, S. Laruelle, S. Grugeon, L. Dupont and J. M. Tarascon, *Nature*, 2000, **407**, 496–499.
3 X. L. Wu, Y. G. Guo, L. J. Wan and C. W. Hu, *J. Phys. Chem. C*, 2008, **112**, 16824–16829.
4 C. Wang, Y. Zhou, M. Y. Ge, X. B. Xu, Z. L. Zhang and J. Z. Jiang, *J. Am. Chem. Soc.*, 2010, **132**, 46–47.
5 D. H. Wang, R. Kou, D. Choi, Z. G. Yang, Z. M. Nie, J. Li, L. V. Saraf, D. H. Hu, J. G. Zhang, G. L. Graff, J. Liu, M. A. Pope and I. A. Aksay, *ACS Nano*, 2010, **4**, 1587–1595.
6 C. K. Chan, H. L. Peng, G. Liu, K. McIlwrath, X. F. Zhang, R. A. Huggins and Y. Cui, *Nat. Nanotechnol.*, 2008, **3**, 31–35.
7 J. X. Zhu, T. Sun, J. S. Chen, W. H. Shi, X. J. Zhang, X. W. Lou, S. Mhaisalkar, H. H. Hng, F. Boey, J. Ma and Q. Y. Yan, *Chem. Mater.*, 2010, **22**, 5333–5339.
8 C. Kim, M. Noh, M. Choi, J. Cho and B. Park, *Chem. Mater.*, 2005, **17**, 3297–3301.
9 S.-L. Chou, J.-Z. Wang, D. Wexler, K. Konstantinov, C. Zhong, H.-K. Liu and S.-X. Dou, *J. Mater. Chem.*, 2010, **20**, 2092–2098.
10 N. Li, G. Liu, C. Zhen, F. Li, L. Zhang and H.-M. Cheng, *Adv. Funct. Mater.*, 2011, **21**, 1717–1722.
11 S. Yang, X. Feng, L. Wang, K. Tang, J. Maier and K. Müllen, *Angew. Chem., Int. Ed.*, 2010, **49**, 4795–4799.
12 S. B. Yang, X. L. Feng, S. Ivanovici and K. Mullen, *Angew. Chem., Int. Ed.*, 2010, **49**, 8408–8411.
13 H. Qiao, L. F. Xiao, Z. Zheng, H. W. Liu, F. L. Jia and L. Z. Zhang, *J. Power Sources*, 2008, **185**, 486–491.
14 J. Y. Xiang, J. P. Tu, L. Zhang, Y. Zhou, X. L. Wang and S. J. Shi, *Electrochim. Acta*, 2010, **55**, 1820–1824.
15 L. Yuan, Z. P. Guo, K. Konstantinov, P. Munroe and H. K. Liu, *Electrochem. Solid-State Lett.*, 2006, **9**, A524–A528.
16 J. Zheng, J. Liu, D. P. Lv, Q. Kuang, Z. Y. Jiang, Z. X. Xie, R. B. Huang and L. S. Zheng, *J. Solid State Chem.*, 2010, **183**, 600–605.
17 H. Xie, Y. Z. Li, S. F. Jin, J. J. Han and X. J. Zhao, *J. Phys. Chem. C*, 2010, **114**, 9706–9712.
18 G. Wang, X. P. Gao and P. W. Shen, *J. Power Sources*, 2009, **192**, 719–723.
19 L. W. Ji and X. W. Zhang, *Electrochem. Commun.*, 2009, **11**, 1146–1149.
20 A. L. M. Reddy, M. M. Shaijumon, S. R. Gowda and P. M. Ajayan, *Nano Lett.*, 2009, **9**, 1002–1006.
21 W. Wang and P. N. Kumta, *ACS Nano*, 2010, **4**, 2233–2241.
22 G. Chen, Z. Y. Wang and D. G. Xia, *Chem. Mater.*, 2008, **20**, 6951–6956.
23 A. Eftekhari and B. Yazdani, *J. Polym. Sci., Part A: Polym. Chem.*, 2010, **48**, 2204–2213.
24 B. J. Li, H. Q. Cao, J. Shao, M. Z. Qu and J. H. Warner, *J. Mater. Chem.*, 2011, **21**, 2069.
25 W. Lv, F. Sun, D.-M. Tang, H.-T. Fang, C. Liu, Q.-H. Yang and H.-M. Cheng, *J. Mater. Chem.*, 2011, **21**, 9014.
26 M. Zhang, D. Lei, Z. Du, X. Yin, L. Chen, Q. Li, Y. Wang and T. Wang, *J. Mater. Chem.*, 2011, **21**, 1673–1676.
27 D. H. Wang, D. W. Choi, J. Li, Z. G. Yang, Z. M. Nie, R. Kou, D. H. Hu, C. M. Wang, L. V. Saraf, J. G. Zhang, I. A. Aksay and J. Liu, *ACS Nano*, 2009, **3**, 907–914.
28 H. Wang, L.-F. Cui, Y. Yang, H. S. Casalongue, J. T. Robinson, Y. Liang, Y. Cui and H. Dai, *J. Am. Chem. Soc.*, 2010, **132**, 13978–13980.
29 G. Zhou, D.-W. Wang, F. Li, L. Zhang, N. Li, Z.-S. Wu, L. Wen, G. Q. Lu and H.-M. Cheng, *Chem. Mater.*, 2010, **22**, 5306–5313.
30 M. S. Park, G. X. Wang, Y. M. Kang, D. Wexler, S. X. Dou and H. K. Liu, *Angew. Chem., Int. Ed.*, 2007, **46**, 750–753.
31 X. M. Yin, C. C. Li, M. Zhang, Q. Y. Hao, S. Liu, L. B. Chen and T. H. Wang, *J. Phys. Chem. C*, 2010, **114**, 8084–8088.
32 H. Uchlyama, E. Hosono, I. Honma, H. Zhou and H. Imai, *Electrochem. Commun.*, 2008, **10**, 52–55.
33 C. H. Xu, J. Sun and L. Gao, *J. Phys. Chem. C*, 2009, **113**, 20509–20513.
34 Z. X. Yang, G. D. Du, C. Q. Feng, S. A. Li, Z. X. Chen, P. Zhang, Z. P. Guo, X. B. Yu, G. N. Chen, S. Z. Huang and H. K. Liu, *Electrochim. Acta*, 2010, **55**, 5485–5491.
35 H. J. Wang, J. M. Wang, W. B. Fang, H. Wan, L. Liu, H. Q. Lian, H. B. Shao, W. X. Chen, J. Q. Zhang and C. N. Cao, *Electrochem. Commun.*, 2010, **12**, 194–197.
36 D. Deng and J. Y. Lee, *Chem. Mater.*, 2008, **20**, 1841–1846.

37 J. S. Chen, C. M. Li, W. W. Zhou, Q. Y. Yan, L. A. Archer and X. W. Lou, *Nanoscale*, 2009, **1**, 280–285.
38 D. W. Kim, I. S. Hwang, S. J. Kwon, H. Y. Kang, K. S. Park, Y. J. Choi, K. J. Choi and J. G. Park, *Nano Lett.*, 2007, **7**, 3041–3045.
39 W. J. Lee, M. H. Park, Y. Wang, J. Y. Lee and J. Cho, *Chem. Commun.*, 2010, **46**, 622–624.
40 J. Liu, W. Li and A. Manthiram, *Chem. Commun.*, 2010, **46**, 1437–1439.
41 X. W. Lou, C. M. Li and L. A. Archer, *Adv. Mater.*, 2009, **21**, 2536–2539.
42 S. M. Paek, E. Yoo and I. Honma, *Nano Lett.*, 2009, **9**, 72–75.
43 H. X. Zhang, C. Feng, Y. C. Zhai, K. L. Jiang, Q. Q. Li and S. S. Fan, *Adv. Mater.*, 2009, **21**, 2299–2304.
44 N. Xiao, X. Dong, L. Song, D. Liu, Y. Tay, S. Wu, L. Li, Y. Zhao, T. Yu, H. Zhang, W. Huang, H. Hng, P. M. Ajayan and Q. Y. Yan, *ACS Nano*, 2011, **5**, 2749–2755.
45 J. X. Zhu, T. Zhu, X. Z. Zhou, Y. Y. Zhang, X. W. Lou, X. D. Chen, H. Zhang, H. H. Hng and Q. Y. Yan, *Nanoscale*, 2011, **3**, 1084–1089.
46 J. P. Liu, Y. Y. Li, H. J. Fan, Z. H. Zhu, J. Jiang, R. M. Ding, Y. Y. Hu and X. T. Huang, *Chem. Mater.*, 2010, **22**, 212–217.
47 W. S. Hummers and R. E. Offeman, *J. Am. Chem. Soc.*, 1958, **80**, 1339.
48 X. Z. Zhou, X. Huang, X. Y. Qi, S. X. Wu, C. Xue, F. Y. C. Boey, Q. Y. Yan, P. Chen and H. Zhang, *J. Phys. Chem. C*, 2009, **113**, 10842–10846.
49 W. Shi, J. Zhu, D. H. Sim, Y. Y. Tay, Z. Lu, X. Zhang, Y. Sharma, M. Srinivasan, H. Zhang, H. H. Hng and Q. Yan, *J. Mater. Chem.*, 2011, **21**, 3422.
50 A. V. Murugan, T. Muraliganth and A. Manthiram, *Chem. Mater.*, 2009, **21**, 5004–5006.
51 D. R. Dreyer, S. Park, C. W. Bielawski and R. S. Ruoff, *Chem. Soc. Rev.*, 2010, **39**, 228–240.
52 Q. Y. Yan, M. S. Raghuveer, H. F. Li, B. Singh, T. Kim, M. Shima, A. Bose and G. Ramanath, *Adv. Mater.*, 2007, **19**, 4358–4363.
53 S. Saadat, Y. Y. Tay, J. X. Zhu, P. F. Teh, S. Maleksaeedi, M. M. Shahjamali, M. Shakerzadeh, M. Srinivasan, B. Y. Tay, H. H. Hng, J. Ma and Q. Y. Yan, *Chem. Mater.*, 2011, **23**, 1032–1038.
54 J. Yao, X. P. Shen, B. Wang, H. K. Liu and G. X. Wang, *Electrochem. Commun.*, 2009, **11**, 1849–1852.
55 R. Yang, W. Zhao, J. Zheng, X. Z. Zhang and X. G. Li, *J. Phys. Chem. C*, 2010, **114**, 20272–20276.
56 Y. Yu, L. Gu, A. Dhanabalan, C. H. Chen and C. L. Wang, *Electrochim. Acta*, 2009, **54**, 7227–7230.
57 H. S. Kim, Y. Piao, S. H. Kang, T. Hyeon and Y. E. Sung, *Electrochem. Commun.*, 2010, **12**, 382–385.
58 H. Liu, G. X. Wang, J. Park, J. Wang and C. Zhang, *Electrochim. Acta*, 2009, **54**, 1733–1736.
59 M. V. Reddy, T. Yu, C. H. Sow, Z. X. Shen, C. T. Lim, G. V. Subba Rao and B. V. R. Chowdari, *Adv. Funct. Mater.*, 2007, **17**, 2792–2799.